Effects of A-site cation structure on the stability of 2D tin halide perovskites

*Tareq Hossain, Harindi R. Atapattu, Henry Pruett, Md Tawabur Rahman, Kevin R. Pedersen, Aron J. Huckaba, Sean R. Parkin, and Kenneth R. Graham**

Department of Chemistry, University of Kentucky, Lexington, Kentucky 40506, USA

ABSTRACT: Two-dimensional halide perovskites (2D-HPs) are of significant interest for their applications in optoelectronic devices. Part of this increased interest in 2D-HPs stems from their increased stability relative to their 3D counterparts. Here, the origin of higher stability in 2D-HPs is mainly attributed to the bulky ammonium cation layers, which can act as a blocking layer against moisture and oxygen ingression and ion diffusion. While 2D-HPs have demonstrated increased stability, it is not clear how the structure of the ammonium ion impacts the material stability. Herein, we investigate how the structure of ammonium cations, including three *n*-alkyl ammoniums, phenethylammonium (PEA) and five PEA derivatives, anilinium (An), benzylammonium (BzA), and cyclohexylmethyl ammonium (CHMA), affects the crystal structure and air, water, and oxygen stability of 2D tin halide perovskites (2D-SnHPs). We find that stability is influenced by several factors, including the molecular packing and intermolecular interactions in the organic layer, steric effects around the ammonium group, the orientation distribution of the 2D sheets, and the hydrophobicity of the perovskite film surface. With superior hydrophobicity, strong interactions between organic layers, and a high extent of parallel oriented inorganic sheets,

the 2-(4-trifluoromethyl-phenyl)-ethylammonium (4-TFMPEA) ion forms the most stable 2D-SnHP among the 12 ammonium cations investigated.

▪ INTRODUCTION

Halide perovskites (HPs) are now-a-days one of the most studied semiconductor materials because of their applications in various technologies, including solar cells,[1-4] high energy radiation detectors,[5-9] light emitting diodes (LEDs),[10-12] photodetectors,[13-15] lasers[16-19] and so forth.[20-22] However, the most efficient HPs contain lead and the toxicity associated with lead can restrict their applications.[23-25] Being in the same group of the periodic table and having a similar ionic radius, Sn is a promising alternative to Pb. Here, Sn-based HPs (Sn-HPs) exhibit comparable structural and optoelectronic properties as lead.[26] In addition to lower toxicity, Sn-HPs are advantageous for their higher charge-carrier mobility and lower band gaps.[27-29] Unfortunately, substituting Pb^{2+} with Sn^{2+} decreases the stability of HPs significantly due to the facile oxidation of Sn^{2+} to Sn^{4+}.[30, 31] The oxidation causes p-type self-doping in the Sn-HPs, resulting in a transition from semiconducting to metallic behavior.[32-35] Interestingly, it has been reported that the p-type doping can be reduced by lowering the dimensionality of the Sn-HPs using bulky organic cations.[36] Furthermore, altering the dimensionality provides another means to tune the optical properties of HPs.

Two-dimensional (2D) Ruddlesden-Popper (RP) organic metal halide perovskites (2D-HPs) have the general formula of $A_2A'_{n-1}M_nX_{3n+1}$.[37] For n=1 phase, a plane of MX_6 (M = Pb^{2+}or Sn^{2+}; X = Cl^-, Br^-, or I^-) corner sharing octahedra is sandwiched between two planes of ammonium cations (A).[38, 39] The chemical structure of the A-site cations plays a crucial role in modifying the crystal structure and tuning the optoelectronic properties of HPs.[40] Here, the M–X bond lengths,

M–X–M bond angles, and octahedral tilts vary with the structure of the A-site cation. For a given metal halide combination, the M–X–M bond angle exerts the strongest influence on the band gap.[41] As the deviation from the ideal 180˚ M–X–M bond angle increases, the band gap increases. For example, Mitzi et al. reported that fluorine substitution at the 2-position of phenethylammonium (PEA) in 2D HPs reduces the Sn–I–Sn bond angle resulting in higher optical gaps.[41] The bulky A-site cations also increase the exciton binding energy and limit charge transport, particularly in the direction perpendicular to the 2D inorganic sheets.[42, 43] Aside from the variations in optical and electronic properties offered with 2D-HPs, another motivating factor for 2D-HPs is their superior ambient stability compared to 3D-HPs.[44-49] This improved stability has driven research into both Pb- and Sn-based 2D-HPs, including the use of 2D-HPs as capping layers on 3D HPs and mixed 2D/3D HPs for photovoltaic applications.[50-52] Recently, Sn-based 2D-HPs (2D-SnHPs) have been used in field effect transistors (FETs),[53-57] LEDs,[58-61] lasers,[62-64], photodetectors,[65-67] and X-ray detectors.[68, 69]

As with the structural and optoelectronic properties of HPs, the A-site cation also influences the stability of HPs. Generally, the moisture resistance of HPs increases with the hydrophobicity of the A-site cation.[70] For example, fluorination of A-site cations increases the hydrophobicity of HPs and thus increases their stability.[39, 67, 71-73] In addition to hydrophobicity, the interaction strength between the A-site cations and the A-site packing density appear to have a large impact on stability.[74-77] For example, A-site cations with phenyl groups tend to form more stable HPs than A-site cations with linear alkyl chains.[67] However, a comprehensive understanding of how the structure of A-site cations affects the air, oxygen, and moisture stability of 2D-HP thin films is currently lacking.

In this study we use a series of ammonium cations to determine how the stability of 2D-SnHPs depends on the A-site cation structure. We first experimentally determine the crystal structures using single crystal X-ray diffraction (SCXRD) to gauge how the structure of the ammonium cation influences the bond angles and octahedral distortion in the inorganic sheets, as well as the intermolecular interactions between the A-site cations and the packing density. Thin films of the 2D HPs are then investigated to determine the orientation distribution of the 2D inorganic sheets with respect to the substrate using grazing-incidence small-angle X-ray scattering (GISAXS), while the hydrophobicity and morphology of 2D-SnHP thin films are probed using contact angle measurements and scanning electron microscopy (SEM), respectively. The degradation of 2D-SnHPs in air, oxygen, and moisture are probed using UV-Vis absorbance spectroscopy in a controlled atmosphere chamber to determine how the aforementioned material and film properties impact stability.

▪ EXPERIMENTAL SECTION

Materials. Tin powder (99.8%, Sigma Aldrich), tin (II) iodide (99.9%, Alfa Aesar), anilinium iodide (AnI, >98.0%, TCI), 2-(4-trifluoromethyl-phenyl)-ethylamine (Oakwood Chemical), 2-(2-(trifluoromethyl-phenyl)-ethylamine (95%, Thermo Scientific Chemicals), 2-(2-fluorophenyl)ethylamine (>98.0%, TCI), diethyl ether (DEE, 98%, VWR Chemicals BDH), tin (II) oxide (SnO, 99.9% trace metal basis, BTC), ethanol (denatured, VWR Chemicals BDH), hypophosphorous acid (50% w/w aqueous solution, ThermoFisher Scientific) and hydroiodic acid (HI, 57% w/w aqueous solution, ThermoFisher Scientific) were used as purchased without further purification. Phenethylammonium iodide (PEAI), 4-fluorophenethylammonium iodide (4-FPEAI), 4-methoxyphenethylammonium iodide (4-MeOPEAI), benzylammonium iodide (BzAI), cyclohexylmethylammonium iodide (CHMAI), n-butylammonium iodide (n-BAI), n-

pentylammonium iodide (n-PAI), and n-hexylammonium iodide (n-HAI) were purchased from Greatcell Solar and used without further purification. N, N-dimethylformamide (DMF, 99.98%, anhydrous, DriSolv) was degassed through freeze-pump-thaw cycling and dried using dry molecular sieve.

Synthesis of ammonium iodides. 1 g of the amines were mixed with 10 mL of ethanol in a 25 mL round-bottom flask and cooled in an ice bath for 10 minutes. Equimolar HI was added dropwise to the amine solution under continuous stirring. The mixture was stirred for 2 hours. Later, the resulting solution was dried using a rotary evaporator at 60 ˚C followed by washing in dry ice-cold DEE. The ammonium iodide crystals were then dried overnight in a vacuum oven at 60 ˚C.

Synthesis of A_2SnI_4 single crystals. The single crystals were synthesized by following a previously published procedure.[63] Briefly, 2.0 mmol of ammonium salts were dissolved in 2 mL of ethanol. In a separate vial, 1.0 mmol of SnO was dissolved in 1.5 mL of HI and 0.4 mL of H_3PO_2 to form SnI_2. The ammonium iodide solution was added to the SnI_2 solution under continuous stirring at 90 ˚C followed by addition of 1.5 mL of ethanol. The vial was transferred to an oil bath and heated at 80 ˚C for an hour. After that the hot plate was turned off and the oil bath was cooled to room temperature naturally to form the crystals.

Fabrication of 2D-SnHP thin films. The precursor solutions were prepared by dissolving appropriate amounts of ammonium iodide salts and SnI_2 in DMF to form 0.3 M A_2SnI_4 solutions. A small amount of excess metallic Sn powder was used, such that insoluble metallic Sn was apparent in solution, to remove any oxidation product of SnI_2 (i.e., SnI_4 and I_2). The precursor solution was heated at 70 ˚C for 30 minutes and filtered with 0.45 μm PTFE syringe filters to

remove insoluble metallic Sn right before spin coating. The precursor solutions were spin coated at 9999 rpm for 30 s on top of pre-cleaned 1″ x 1″ glass substrates inside a nitrogen filled glovebox (0.1 ppm of O_2 and H_2O) followed by annealing at 80 ˚C for 10 minutes. The glass substrates were cleaned by sonicating in sodium dodecyl sulfate solution (0.5 mg/ml in water), deionized (DI) water, acetone, and *iso*-propanol sequentially for 15 minutes. The glass substrates were treated with UV-ozone for 15 minutes and taken to the glovebox immediately before spin coating.

UV-Vis absorbance. The absorbance of A_2SnI_4 thin films was measured using an Ocean Optics QE Pro high-performance fiber optic spectrometer with a thermoelectric cooled CCD detector and a DH-2000 light source from Ocean Optics.

Flow Chamber. In a flow chamber,[30] pure oxygen or 100% humid nitrogen was blown at a flow rate of 0.4 standard cubic feet per minute (SCFM) for 5 minutes or 10 minutes, respectively. The chamber pressure reaches 15 psi for oxygen or 22 psi for humid nitrogen after the flow is stopped. Using two Kodiak Glass view ports light enters and exits the chamber.

Scanning electron microscopy (SEM). Samples were prepared on ITO coated glass substrates by following the same recipe mentioned earlier. The SEM images of A_2SnI_4 thin films were taken using a Helios Nanolab 660/G3 dual beam SEM from ThermoFisher Scientific.

Single crystal X-ray diffraction (SCXRD). X-ray diffraction data were collected at either 90.0(2) or 100.0(2) K on a Bruker D8 Venture kappa-axis diffractometer using Mo Kα X-rays. Raw data were integrated, scaled, merged, and corrected for Lorentz-polarization effects using the APEX3 package. Corrections for absorption were applied using SADABS[78] and XABS2.[79] The structures were solved using iterative dual-space methods (SHELXT)[80] and refinement was carried out against F^2 by weighted full-matrix least-squares (SHELXL).[81] Hydrogen atoms were found in

difference maps and refined using riding models. Non-hydrogen atoms were refined with anisotropic displacement parameters. Atomic scattering factors were taken from the International Tables for Crystallography.[82]

Powder X-ray diffraction (PXRD) and Grazing-incidence small angle X-ray scattering (GISAXS). Measurements were done on A_2SnI_4 thin films fabricated on glass substrates by following the same recipe mentioned earlier. The 1″ x 1″ perovskite coated substrates were broken into 4 pieces before the measurements. PXRD and GISAXS were performed using a Bruker D8 Advance instrument and a Xeuss 2.0 system from Xenocs, respectively. In both measurements a copper anode X-ray source (Cu Kα X-ray, $\lambda = 1.5418$ Å) was used. For GISAXS, the sample stage was tilted by 0.16˚ towards the X-ray source. Data were collected for 500 s with 2θ spanning 1 – 32˚.

Contact angle. The contact angle, i.e. wettability of deionized (DI) water on the 2D-SnHP films, was performed using a Drop Shape Analyzer (DSA25, KRÜSS, Germany) instrument. All measurements were performed at room temperature (approximately 25 °C). The contact angle was measured using a sessile drop of DI water on the solid film and video was recorded of the contact angle change over time. Given that the films dissolve quickly (within seconds) upon contact with DI water, an angle at the solid, liquid, and gas interface was measured after 0.1 seconds of the drop being deposited on the film, except for $(4\text{-TFMPEA})_2SnI_4$ where the contact angle was taken at 0.16 s.

▪ RESULTS AND DISCUSSION

We investigate the effects of A-site cation structure on the stability of 2D-SnHPs using a series of 12 cations depicted in **Figure 1a**. This family of cations enables us to investigate several

variables, including those related to both steric and electrostatic interactions. PEA and its derivatives are used to probe the impact of 2- vs. 4- substitutions on the stability, with the size and electron withdrawing strength of the substituents varied. To investigate the steric effects near the ammonium group, BzA and An are employed to decrease the separation between the phenyl and ammonium groups. Cyclohexylmethylammonium (CHMA) is included as a non-aromatic analog to BzA to probe the impact of planar vs. non-planar cyclic cations on the stability of 2D-SnHPs, while three *n*-alkyl ammonium cations are used to further vary the A-site packing and inter-sheet spacing, as illustrated in **Figure 1b**.

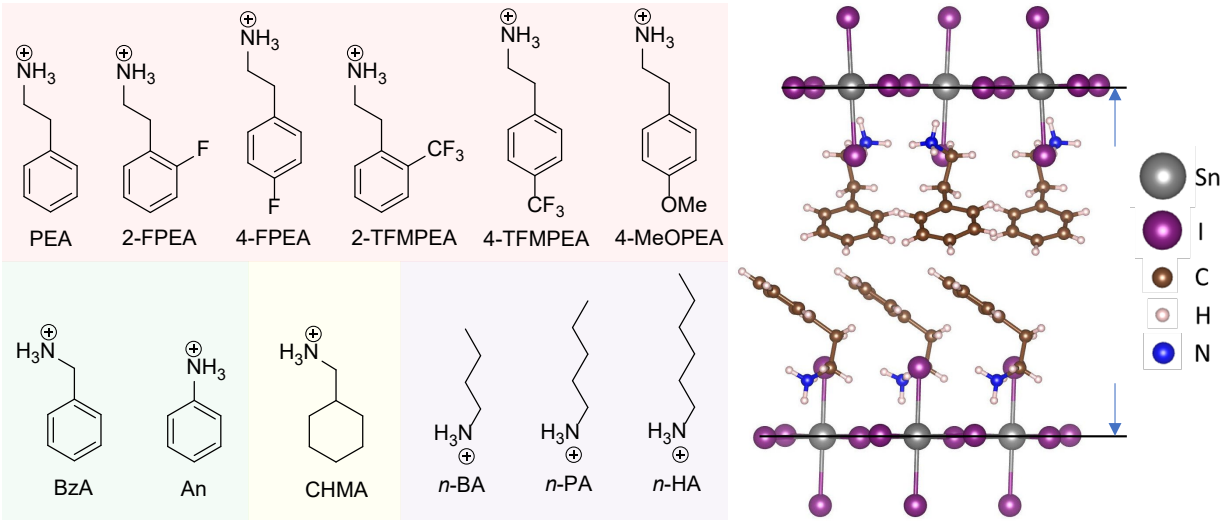

Figure 1: (a) A-site cations incorporated into 2D-SnHPs. (b) Crystal structure of $(PEA)_2SnI_4$ illustrating the inter-sheet spacing (d_{IS}).

We grew single crystals of A_2SnI_4 HPs and performed SCXRD to probe how the A-site cation structure affects the crystal structure (**Figure 2, and Figure S1**). Relevant crystal parameters are summarized in **Table 1**. We find that all synthesized A_2SnI_4 single crystals form RP-phase 2D HPs. By varying the A-site cation structure, the Sn–I–Sn bond angle, Sn–I bond length, and inter-

sheet spacing (d_{IS}) can be tuned.[83] Depending on the A-site cation structure the Sn–I–Sn bond angle varies from 148.55˚ to 160.59˚, with $(2\text{-TFMPEA})_2SnI_4$ and $(BzA)_2SnI_4$ displaying the smallest and largest bond angles, respectively. The 2D-SnHPs with PEA derivatives substituted at the 2 position (2-PEAs) have smaller Sn–I–Sn bond angles compared to PEA derivatives with substituents at the 4 position (4-PEAs), where the bond angle with the 2-PEAs decreases as the size of the substituent increases. These bond angle variations are largely explained through accounting for steric effects. Unfortunately, we were not able to synthesize single crystals of $(4\text{-TFMPEA})_2SnI_4$, and $(An)_2SnI_4$; thereby, we include the inferred d_{IS} from the PXRD spectra.

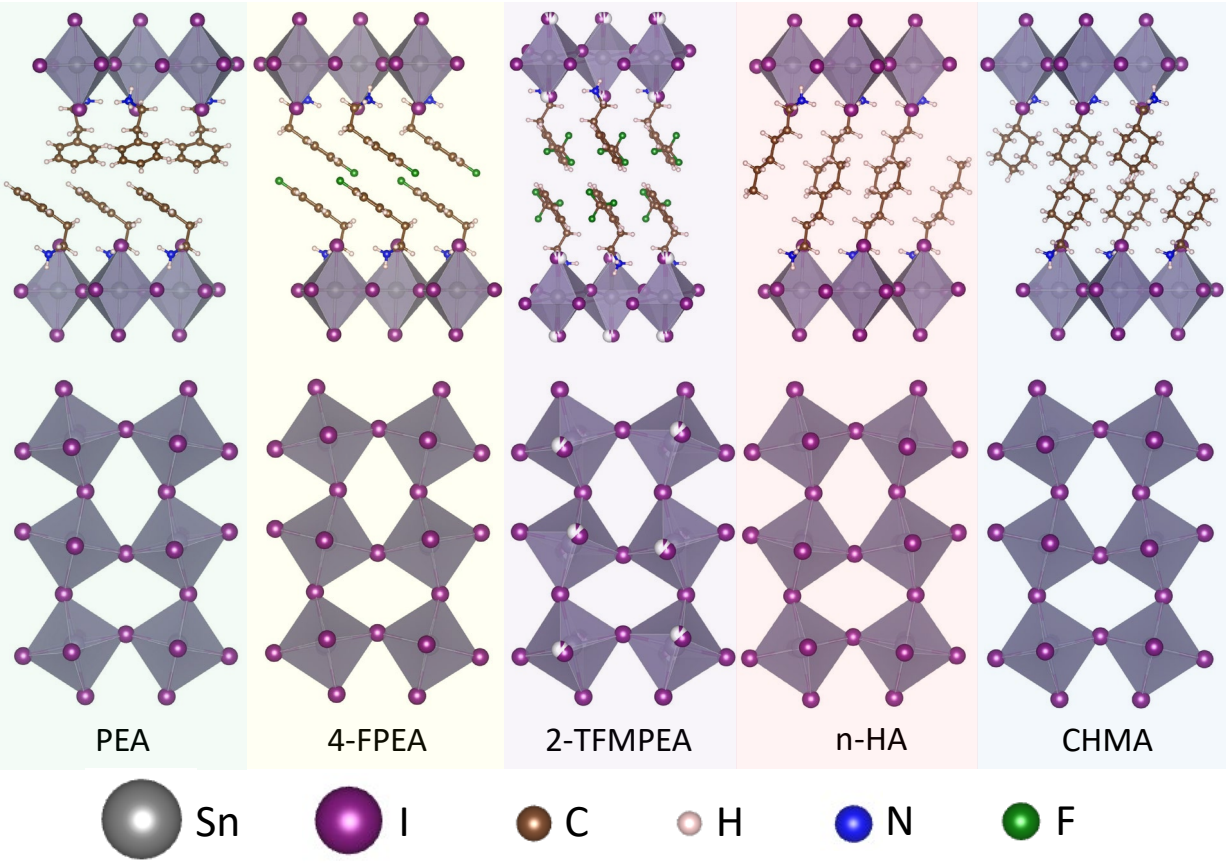

Figure 2: Crystal structures of A_2SnI_4 with different A-site cations. The view along the plane of the 2D inorganic sheets is shown in the top row and the view perpendicular to that plane in the bottom row with the A-site cations removed in the bottom row for clarity.

Thin films of A_2SnI_4 on clean glass substrates were fabricated and characterized using PXRD (**Figure S2**). Here, all PXRD patterns show a dominant peak associated with diffraction from the 2D inorganic sheets, e.g., the (002) plane in PEA_2SnI_4, which is typical for A_2SnI_4 films.[58, 66] To correlate SCXRD data with the measurements done on the thin films we compare the calculated powder diffraction pattern from SCXRD with the PXRD pattern measured on thin films (**Figure S2**) and we observe peak shifts in the range of 2θ of 0.02 to 0.20°, with the films showing slightly increased d_{IS} (0.05-0.62 Å) relative to the single crystals.

Table 1: Crystal structure parameters obtained from SCXRD measurements, unless otherwise noted.

Compound	Sn–I–Sn bond angle[#] (deg)	Eq/Ax Sn–I bond length[#] (Å)	Inter-sheet spacing (Å)	Sn-I bond length distortion index	N–H···I bond distance[¶] (Å)
$(PEA)_2SnI_4$	155.93 ± 0.52	3.123 ± 0.008/ 3.161 ± 0.000	16.010	0.0053	2.798 ± 0.061
$(2\text{-FPEA})_2SnI_4$	151.43 ± 0.32	3.131 ± 0.027/ 3.179 ± 0.199	16.305	0.0265	2.801 ± 0.108
$(4\text{-FPEA})_2SnI_4$	155.46 ± 0.00	3.113 ± 0.003/ 3.165 ± 0.000	16.185	0.0074	2.793 ± 0.072
$(2\text{-TFMPEA})_2SnI_4$	148.55 ± 0.00	3.117 ± 0.000/ 3.149 ± 0.000	19.044	0.0046	2.724 ± 0.069
$(4\text{-TFMPEA})_2SnI_4$[*]	N/A	N/A	18.108	N/A	N/A
$(4\text{-MeOPEA})_2SnI_4$	154.14 ± 0.71	3.123 ± 0.024/ 3.199 ± 0.209	17.673	0.0288	2.827 ± 0.075
$(BzA)_2SnI_4$[**]	160.59 ± 0.00	3.186 ± 0.009/ 3.156 ± 0.000	14.394	0.0041	2.884 ± 0.158
$(An)_2SnI_4$[*]	N/A	N/A	13.515	N/A	N/A
$(n\text{-HA})_2SnI_4$	158.04 ± 0.00	3.129 ± 0.006/ 3.177 ± 0.000	16.068	0.0066	2.805 ± 0.133
$(n\text{-PA})_2SnI_4$	153.84 ± 0.00	3.147 ± 0.007/ 3.127 ± 0.000	14.394	0.0028	2.815 ± 0.028
$(n\text{-BA})_2SnI_4$[**]	159.61 ± 0.00	3.148 ± 0.014/ 3.138 ± 0.000	13.810	0.0037	2.836 ± 0.130

$(CHMA)_2SnI_4$	155.52 ± 0.00	3.117 ± 0.02/ 3.168 ± 0.000	16.305	0.0074	2.751 ± 0.074

*Inter-sheet spacing obtained from PXRD measurements.
**Crystal structures for $(BzA)_2SnI_4$ and $(n\text{-}BA)_2SnI_4$ were taken from the literature.[84, 85]
#Error values represent standard deviations from all bond lengths or angles. Eq is equatorial and Ax is axial.
¶Error values represent standard deviations from the three shortest N–H···I bonds.
ǂBond length distortion index is calculated using this equation: $\frac{1}{n}\sum_{n=1}^{6}\frac{|di-do|}{do}$, where d_i is the individual bond lengths and d_o is the average bond length.

To probe the effect of A-site cation structure on the optical properties of A_2SnI_4 thin films, we measured their UV-vis absorbance spectra (**Figure S3**). All A_2SnI_4 films show three characteristic absorbance peaks of 2D-SnHPs with variations in peaks positions. The peak shifts in absorbance spectra are mainly due to the variation in Sn–I–Sn bond angle between corner sharing octahedra. Here, as the Sn–I–Sn bond angle decreases the optical gap increases.[41] For example, $(2\text{-}TFMPEA)_2SnI_4$ has the smallest Sn–I–Sn bond angle of 148.55° and correspondingly shows the most blue-shifted absorbance peaks.

In 2D-SnHP thin films the crystalline grains often adopted a preferred orientation with the inorganic sheets oriented parallel to the substrate.[86] It is important to find out how the A-site cation structure affects the orientation of the inorganic sheets, as we expect the orientation of the inorganic sheets will significantly affect the ambient stability of 2D-SnHPs. For example, if the organic layers impede water or oxygen diffusion, then increased stability would arise when the sheets are oriented parallel to the substrate. Using GISAXS we probed the orientation of the inorganic sheets (**Figure 3**). We find that the structure of the A-site cations indeed affects the orientation distribution of the inorganic sheets. Comparing PEA and its derivatives, the 4-PEAs show a narrower distribution of orientations, with 63 to 92% of the total detected X-ray intensity diffracted by the inorganic sheets falling between 70 and 80°, as shown in **Table S1**. On the other hand, the 2-PEAs show a broader distribution of inorganic sheet orientations, with only 44 to 55%

of the total detected inter-sheet diffraction intensity falling between 70 and 80°. For 2-PEA derivatives, the inorganic planes become more isotropically oriented as the size of the substituent at the 2-position increases. Contrarily, for 4-PEA derivatives the inorganic planes become more preferentially oriented parallel to the substrate as the size of the substituent increases, with (4-TFMPEA)$_2$SnI$_4$ and (4-FPEA)$_2$SnI$_4$ displaying 92 and 69% of their total detected first peak intensity in the 70-80° range, respectively. Sterics near the ammonium also play a role in the distribution of orientations present, as An is the most isotropically oriented with only 33% of the total detected intensity falling in the 70-80° range.

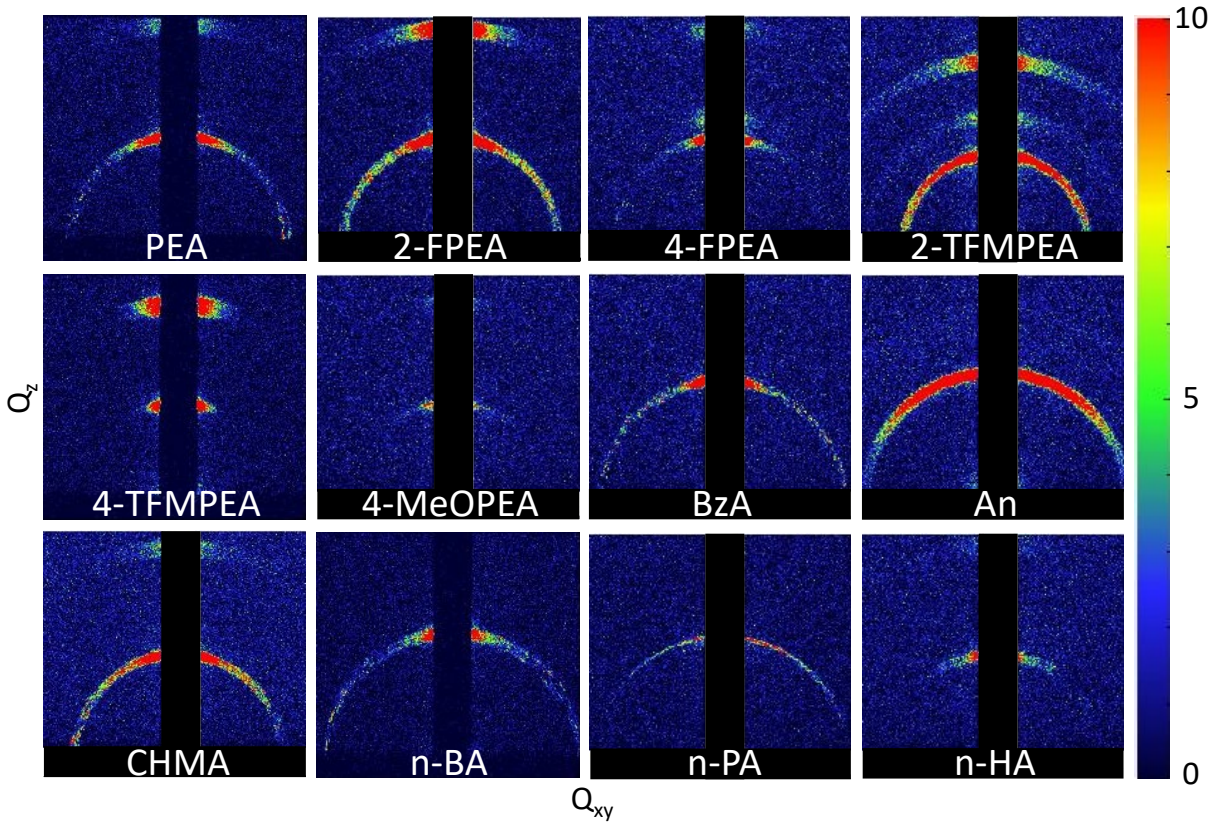

Figure 3: GISAXS images of A$_2$SnI$_4$ thin films fabricated on glass substrates.

A major advantage of 2D HPs relative to 3D HPs is the improved stability and the extensive ability to tune stability based on the A-site molecular structure. To investigate how the structure

of the A site cation affects the stability of A_2SnI_4 films, we exposed these films to air and measured their absorbance at varying times (**Figure 4a**). Here, the integrated intensity of the lowest energy excitonic peak is used as a gauge of stability. A few major stability trends are apparent from this data. First, the stability of the A_2SnI_4 films increases as we change the A-site cation from *n*-alkyl to aromatic. Second, the stability increases significantly as the steric hindrance near the ammonium group decreases, as exemplified by the increasing stability in moving from An to BzA to PEA. Third, PEA derivatives substituted at the 4-position demonstrate improved stability as compared to their counterparts substituted at the 2-position.

One of the most apparent trends is that the *n*-alkyl ammonium cations lead to much worse stability than their PEA counterparts. For example, after 2 hours of continuous air exposure ($(n\text{-HA})_2SnI_4$ retains only 19% of its initial absorbance whereas $(PEA)_2SnI_4$ retains 97%. As shown in **Figure 4a**, all *n*-alkyl containing 2D-SnHPs degrade much faster than the other materials, including faster than with the most sterically hindered ammonium (An). There does not appear to be a strong correlation between crystal structure and degradation for these *n*-alkyl ammoniums. Here, the Sn-I-Sn bond angle spans a reasonably large 6° range and the inter-sheet distance varies by over 2.2 Å, yet the stability remains similarly poor. Furthermore, these bond angles and inter-sheet distances are comparable to the much more stable 2D-SnHPs. The extent of horizontally oriented sheets also does not play a major role, as $(n\text{-HA})_2SnI_4$ displays a large fraction of inorganic sheets oriented parallel to the substrate. Similarly, film morphology is not a determining factor, as the *n*-alkyl containing 2D-SnHPs show some of the most uniform films with large grains (**Figure S4**). The most likely reason for the rapid degradation observed for the *n*-alkyl ammoniums is thereby attributed to a relatively low interlayer-space-filling[76] leading to increased accessibility of oxygen and moisture to the more reactive SnI_4 sheets. This claim is partly supported by

comparison to the 2D-SnHP with the cyclic-alkyl ammonium, CHMA. Here, CHMA shows significantly higher stability compared to *n*-alkyl ammoniums, with the primary difference being that CHMA should more sterically hinder access to the SnI_4 sheets.

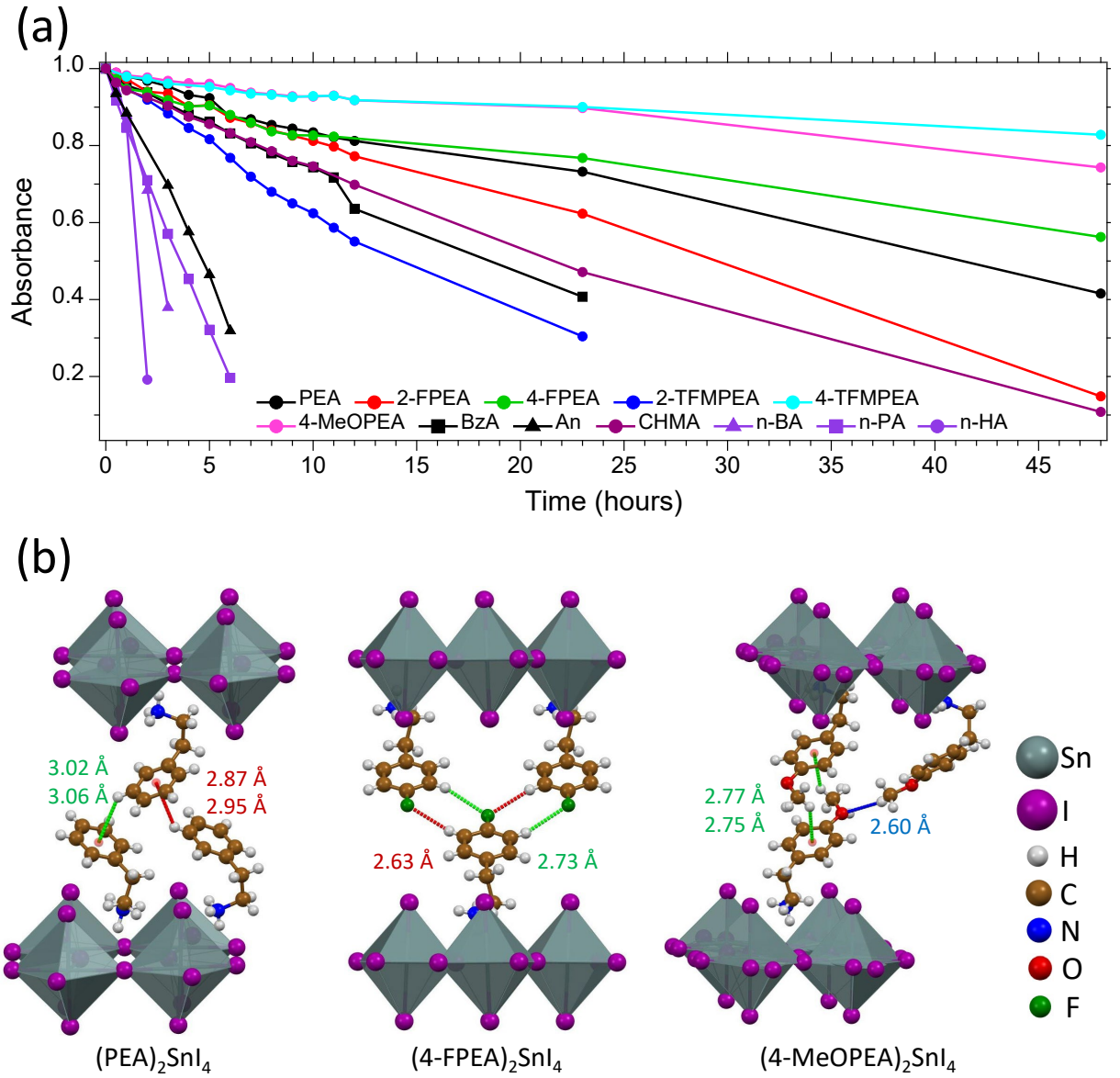

Figure 4: (a) Absorbance intensity vs. time for A_2SnI_4 thin films in air with relative humidity (RH) 20% at 22 ˚C. (b) Illustration of different bonding interactions between the A-site cations of $(PEA)_2SnI_4$, $(4\text{-FPEA})_2SnI_4$, and $(4\text{-MeOPEA})_2SnI_4$. For better visualization minor distortion components are removed from the $(4\text{-MeOPEA})_2SnI_4$ crystal structure.

The stability of the A_2SnI_4 films decreases as steric hindrance around the ammonium group increases. This decrease in stability is exemplified through comparison of An, BzA, and PEA, where the spacing between the ammonium group and the phenyl group increases from 0 to 1 to 2 carbons. For this series, the most sterically hindered An shows far lower stability than both BzA and PEA. Here, $(An)_2SnI_4$ retains only 32% of its initial absorbance after 6 hours of continuous air exposure, while $(PEA)_2SnI_4$ and $(BzA)_2SnI_4$ retain 87 and 83% of their initial absorbance, respectively. The steric trend in comparing PEA and BzA becomes more pronounced at higher air exposure times, with $(PEA)_2SnI_4$ retaining 73% of its initial absorbance compared to only 41% for $(BzA)_2SnI_4$ after 23 hours of continuous air exposure. The most probable reasons for the lower stability of $(BzA)_2SnI_4$ are longer Sn–I and N–H···I bond distances (**Table 1**) and weaker interplanar interactions as evident by the longer CH···π bond distances (**Figure S5**) compared to $(PEA)_2SnI_4$ (**Figure 4b**).

As $(PEA)_2SnI_4$ is comparatively more stable, next we investigate how 2- and 4- substitution on PEA affects the stability of A_2SnI_4. We find that PEA forms a more stable perovskite than the 2-PEA derivatives. After 23 hours of continuous air exposure the $(PEA)_2SnI_4$, $(2\text{-FPEA})_2SnI_4$, and $(2\text{-TFMPEA})_2SnI_4$ retain 73, 62, and 30% of their initial absorbance respectively (**Figure 4a**). These trends also suggest that the stability decreases as the size of the substituent at the 2-position increases. On the other hand, A_2SnI_4 with 4-PEAs are more stable than $(PEA)_2SnI_4$, with larger substituents resulting in increased stability. This trend is illustrated by comparing the absorbance data after 23 hours of continuous air exposure, where $(PEA)_2SnI_4$, $(4\text{-FPEA})_2SnI_4$, $(4\text{-TFMPEA})_2SnI_4$, and $(4\text{-MeOPEA})_2SnI_4$ retain 73, 77, 90, and 90% of their initial absorbance, respectively. After 48 hours of air exposure $(4\text{-TFMPEA})_2SnI_4$ emerges as the most air stable of the 2D HPs tested.

Possible reasons for the decreased stability of 2-PEA containing perovskites compared to $(PEA)_2SnI_4$ include a more isotropic distribution of inorganic sheet orientations with respect to the substrate, as previously discussed (**Figure 3 and Table S1**) and increased octahedral tilting (**Table 1**). Higher octahedral tilting could be an indication of lower thermodynamic stability. Octahedral tilting can be estimated from the Sn–I–Sn bond angle, where lower Sn–I–Sn bond angles indicate increased octahedral tilting. The Sn–I–Sn bond angles in $(PEA)_2SnI_4$, $(2\text{-}FPEA)_2SnI_4$, and $(2\text{-}TFMPEA)_2SnI_4$ are 155.93, 151.43, and 148.55˚ respectively.

For 4-PEA containing perovskites, the most likely reasons for higher stability compared to $(PEA)_2SnI_4$ include an increased extent of inorganic sheets oriented parallel to the substrate, increased interaction strengths between the organic molecules in the interlayer, and tighter packing between A-site cations. For example, using density functional theory (DFT) calculations Mosconi et al. showed that with increasing intermolecular interactions between A-site cations the thermodynamic stability of the 2D-HPs increases.[75] In agreement with their calculations, our experimental data show that as the interaction strength between the A-site cations increases, as evident by shorter contacts and tighter packing, the stability of the 2D-HP increases. For example, the CH···π interaction in $(PEA)_2SnI_4$ is weaker as the average CH···π distance (2.98 Å) is longer than the average CH···FC distance (2.68 Å) in $(4\text{-}FPEA)_2SnI_4$ (**Figure 4b**). Also, each 4-FPEA forms twice the number of interactions compared to PEA. In $(4\text{-}MeOPEA)_2SnI_4$ the shorter CH···π (2.76 Å) distance indicates a stronger interaction between 4-MeOPEA molecules compared to PEA. In addition to the CH···π interaction, 4-MeOPEA has additional C_2O···HC (2.60 Å) interactions with short contacts (**Figure 4b)**.

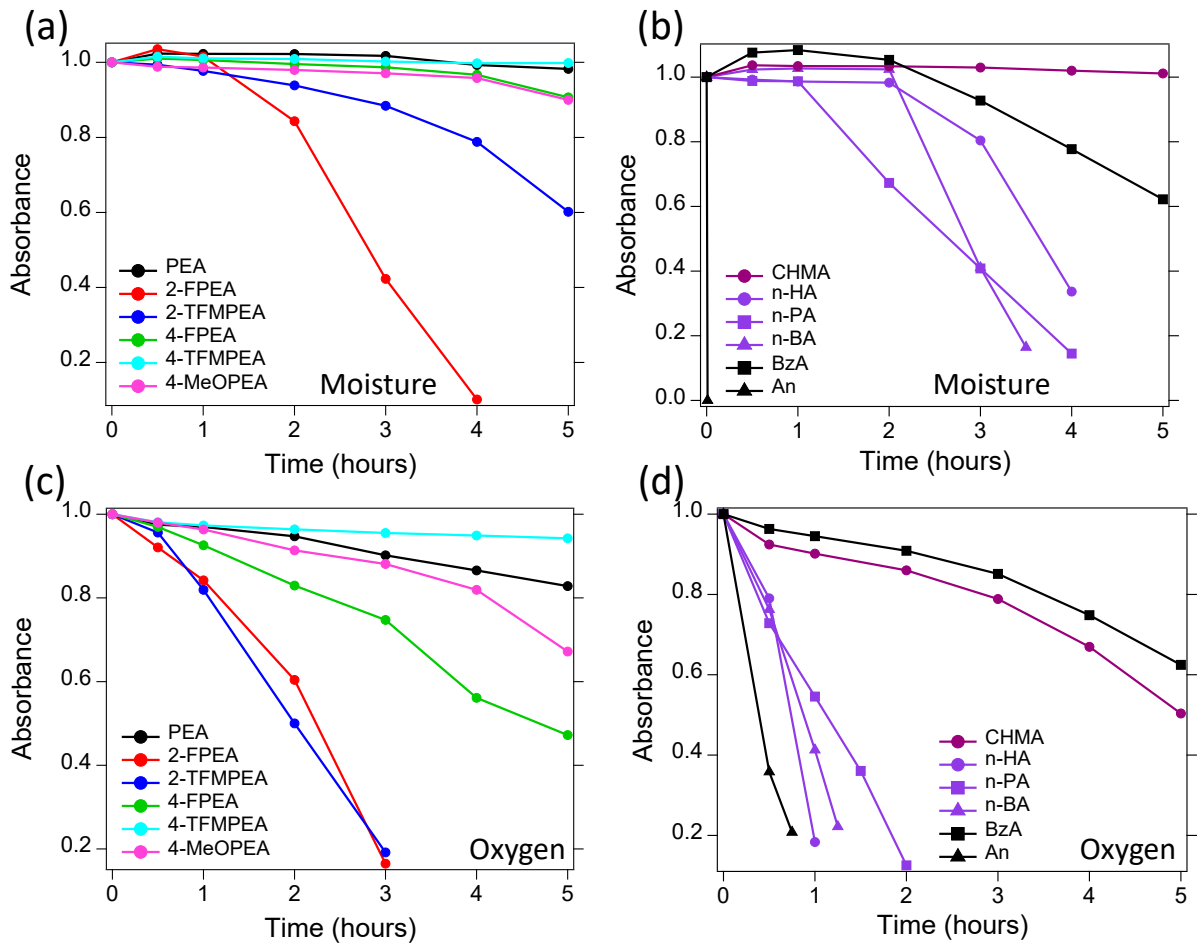

Figure 5: Absorbance intensity vs. time for A_2SnI_4 thin films under humid nitrogen (a, b) and oxygen (c, d) inside a controlled atmosphere chamber.

Now that we have a clear picture of how the air stability of A_2SnI_4 thin films varies with A-site cation structure, next we investigate how A-site cation structure influences the stability of A_2SnI_4 films when exposed to dry oxygen or 100% humid nitrogen (**Figure 5**). Interestingly, we notice a few significant differences in the stability trends for air, oxygen, or humid nitrogen conditions. First, in oxygen or humid nitrogen the stability of $(4\text{-FPEA})_2SnI_4$ and $(4\text{-MeOPEA})_2SnI_4$ are lower than $(PEA)_2SnI_4$, contrarily these are both more stable than $(PEA)_2SnI_4$ in air. Second, the rate of degradation in pure oxygen is overall higher than in humid nitrogen.

This more rapid degradation under oxygen is consistent with previous reported degradation mechanisms and our previous findings that SnI_2 oxidizes more rapidly upon oxygen exposure.[30, 87]

Hydrophobicity, as highlighted by the contact angle measurements in **Figure S6**, is another parameter that we investigated. However, hydrophobicity does not correlate strongly with the air stability data, as depicted in **Figure S6b**. The lack of correlation between air stability and hydrophobicity may arise from oxygen being the primary source, or instigator, of degradation. For example, the $(CHMA)_2SnI_4$ film exhibits the highest stability against water among the perovskites used in this study, yet it is not one of the top performers in terms of stability under oxygen or air exposure. After 5 hours of continuous humid nitrogen exposure $(CHMA)_2SnI_4$ retains 101% of its initial absorbance. The highest moisture stability exhibited by $(CHMA)_2SnI_4$ can be attributed to its superior hydrophobicity compared to the other 2D-SnHP thin films, as indicated by its large contact angle of 96°. On the other hand, after 5 hours of continuous oxygen exposure $(CHMA)_2SnI_4$ retains only 50% of its initial absorbance. Therefore, it seems that increased hydrophobicity can significantly affect moisture stability while having minimal to no influence on oxygen and air stability. We also find that the water stability trend does not completely agree with the hydrophobicity of perovskite films, indicating that stability is often not as simple as the degree of hydrophobicity. For example, after 5 hours of humid nitrogen exposure $(PEA)_2SnI_4$ and $(2\text{-}TFMPEA)_2SnI_4$ retain 98 and 60% of their initial absorbance, which is opposite of what their contact angles of 55 and 64˚, respectively, would predict.

When the A_2SnI_4 thin films are exposed to humid nitrogen most of them show a small increase in absorbance initially (**Figure 5a, b**). Moisture exposure of perovskite films can trigger secondary crystal growth from harmful defects resulting in better morphology and crystallinity of the

perovskite films,[88-90] which could explain the initial increase in absorbance intensity. The $(BzA)_2SnI_4$ thin film exposed to 30 minutes of humid nitrogen shows an enhancement in the PXRD peak intensities compared to the pristine $(BzA)_2SnI_4$ film (**Figure S7**), which further supports our claim. Upon prolonged exposure to moisture, water induces irreversible chemical reactions to perovskites forming volatile amines and hydroiodic acid.[91-93] When these moisture exposed perovskites are thermally annealed on a hot plate in a nitrogen filled glovebox, they do not recover back to their initial absorbance, hence further supporting the water induced irreversible degradation reactions (**Figure S8**). Interestingly, the A_2SnI_4 films show red shifts of their absorbance peaks with continuous moisture exposure (**Figure S9**). We notice a direct relation between moisture induced degradation of perovskite films and the red shift of absorbance peaks. As the moisture induced degradation of A_2SnI_4 films increases, the red shift of the absorbance peaks increases (**Figure S10-21a**). The red shift in the absorbance peaks could indicate that the Sn–I–Sn bond angles have increased and there is better overlap between the 2s orbital of tin and 5p orbital of iodine.[83]

▪ CONCLUSION

This work clearly shows that the stability of 2D-SnHPs can be significantly enhanced by proper choice of A-site cations and provides guidance for selecting and designing bulky ammonium cations for improved stability. We have identified several major parameters that influence the stability of 2D-SnHP films. The most important parameter is the extent that the A-site cations will restrict moisture and oxygen access to the inorganic sheets. Here, more bulky groups, such as phenyl or cyclohexyl groups, that pack densely with strong intermolecular interactions are most effective at stabilizing the 2D-SnHPs. For example, $(4\text{-MeOPEA})_2SnI_4$ and $(4\text{-FPEA})_2SnI_4$ exhibit strong intermolecular interactions and show the second and third highest stability under air

exposure, respectively. The ammonium should not be too sterically hindered however, as the stronger ammonium–iodide interactions are beneficial for increasing stability and smaller Sn–I–Sn bond angles resulting from steric effects reduce stability. From a thin film perspective, the orientation distribution of the 2D inorganic sheets with respect to the substrate and the hydrophobicity of the 2D-SnHP film surface are influential in determining the stability. All these parameters can be tuned by changing the chemical structure of A-site cations. Overall, we find that $(4\text{-TFMPEA})_2SnI_4$ demonstrates the highest stability in air, followed by $(4\text{-MeOPEA})_2SnI_4$ and $(4\text{-FPEA})_2SnI_4$, with these high stabilities arising from a combination of beneficial parameters. It is also likely that processing conditions and substrate chemistries to change the surface energy can be used to alter the distribution of the inorganic sheets, thereby enabling further insight into the role of the orientation distribution on stability. While this work focuses solely on n=1 HPs, we expect that these findings will also largely apply to higher n number 2D-HPs.

ASSOCIATED CONTENT

Supporting Information. Crystal structure views of A_2SnI_4, calculated and experimental PXRD of A_2SnI_4 films, SEM images of A_2SnI_4 films, absorbance spectra of unexposed A_2SnI_4 films, absorbance tracking of A_2SnI_4 films in oxygen and humid nitrogen environments, GISAXS data. CIF files of the reported crystal structures can be found in CCDC with deposition numbers 2392243 (4-FPEA_2SnI_4), 2392244 (HA_2SnI_4), 2392245 (PA_2SnI_4), 2392246 (2-TFMPEA_2SnI_4), 2392247 ($CHMA_2SnI_4$), 2392248 (2-FPEA_2SnI_4), 2392249 ($PEAI_2SnI_4$), 2392250 (4-MeOPEA_2SnI_4).

AUTHOR INFORMATION

Corresponding Author

Kenneth R. Graham - Department of Chemistry, University of Kentucky, Lexington, Kentucky 40506, USA; E-mail: Kenneth.graham@uky.edu

Author Contributions

The manuscript was written through contributions of all authors. All authors have given approval to the final version of the manuscript.

Funding Sources

National Science Foundation: DMR-2102257, NNCI-2025075, 1849213, CHE-1625732.

Notes

The authors declare no competing financial interest.

ACKNOWLEDGMENT

T. H., H. A., H. P., K. P. and K. R. G. acknowledge support from the National Science Foundation (DMR-2102257) for supporting this work. This work was performed in part at the U.K. Electron Microscopy Center, a member of the National Nanotechnology Coordinated Infrastructure (NNCI), which is supported by the National Science Foundation (NNCI-2025075). M.T.R. and A.J.H acknowledge support from the National Science Foundation under Cooperative Agreement

No. 1849213 for supporting this work. S.R.P. thanks the National Science Foundation MRI (CHE-1625732) for single-crystal diffractometer funding.

REFERENCES

(1) Park, S. M.; Abtahi, A.; Boehm, A. M.; Graham, K. R. Surface Ligands for Methylammonium Lead Iodide Films: Surface Coverage, Energetics, and Photovoltaic Performance. *Acs Energy Lett* **2020**, *5* (3), 799-806. DOI: 10.1021/acsenergylett.0c00054.
(2) Park, S. M.; Wei, M.; Lempesis, N.; Yu, W.; Hossain, T.; Agosta, L.; Carnevali, V.; Atapattu, H. R.; Serles, P.; Eickemeyer, F. T.; Shin, H.; Vafaie, M.; Choi, D.; Darabi, K.; Jung, E. D.; Yang, Y.; Kim, D. B.; Zakeeruddin, S. M.; Chen, B.; Amassian, A.; Filleter, T.; Kanatzidis, M. G.; Graham, K. R.; Xiao, L.; Rothlisberger, U.; Grätzel, M.; Sargent, E. H. Low-loss contacts on textured substrates for inverted perovskite solar cells. *Nature* **2023**, *624* (7991), 289-294. DOI: 10.1038/s41586-023-06745-7.
(3) Uddin, M. A.; Hossain, T.; Kothalawala, N. L.; Joy, S.; Kim, D. Y.; Graham, K. R. Multifunctional Thiol-Containing Additives for Improved Photoluminescence and Photovoltaic Performance of CsFAPbI Perovskites. *Acs Appl Electron Ma* **2022**, *4* (3), 903-909. DOI: 10.1021/acsaelm.1c01318.

(4) Yang, Y.; Liu, C.; Ding, Y.; Ding, B.; Xu, J.; Liu, A.; Yu, J.; Grater, L.; Zhu, H.; Hadke, S. S.; Sangwan, V. K.; Bati, A. S. R.; Hu, X.; Li, J.; Park, S. M.; Hersam, M. C.; Chen, B.; Nazeeruddin, M. K.; Kanatzidis, M. G.; Sargent, E. H. A thermotropic liquid crystal enables efficient and stable perovskite solar modules. *Nature Energy* **2024**. DOI: 10.1038/s41560-023-01444-z.
(5) He, Y. H.; Hadar, I.; Kanatzidis, M. G. Detecting ionizing radiation using halide perovskite semiconductors processed through solution and alternative methods. *Nat Photonics* **2022**, *16* (1), 14-26. DOI: 10.1038/s41566-021-00909-5.
(6) Kim, Y. C.; Kim, K. H.; Son, D. Y.; Jeong, D. N.; Seo, J. Y.; Choi, Y. S.; Han, I. T.; Lee, S. Y.; Park, N. G. Printable organometallic perovskite enables large-area, low-dose X-ray imaging. *Nature* **2017**, *550* (7674), 87. DOI: 10.1038/nature24032.
(7) Pan, L.; Liu, Z.; Welton, C.; Klepov, V. V.; Peters, J. A.; De Siena, M. C.; Benadia, A.; Pandey, I.; Miceli, A.; Chung, D. Y.; Reddy, G. N. M.; Wessels, B. W.; Kanatzidis, M. G. Ultrahigh-Flux X-ray Detection by a Solution-Grown Perovskite CsPbBr₃ Single-Crystal Semiconductor Detector. *Advanced Materials* **2023**, *35* (25), 2211840. DOI: 10.1002/adma.202211840.
(8) Pan, L.; Shrestha, S.; Taylor, N.; Nie, W. Y.; Cao, L. R. Determination of X-ray detection limit and applications in perovskite X-ray detectors. *Nat Commun* **2021**, *12* (1). DOI: 10.1038/s41467-021-25648-7.

(9) Wei, H. T.; Huang, J. S. Halide lead perovskites for ionizing radiation detection. *Nat Commun* **2019**, *10*. DOI: 10.1038/s41467-019-08981-w.

(10) Gong, X. W.; Voznyy, O.; Jain, A.; Liu, W. J.; Sabatini, R.; Piontkowski, Z.; Walters, G.; Bappi, G.; Nokhrin, S.; Bushuyev, O.; Yuan, M. J.; Comin, R.; McCamant, D.; Kelley, S. O.; Sargent, E. H. Electron-phonon interaction in efficient perovskite blue emitters. *Nat Mater* **2018**, *17* (6), 550-+. DOI: 10.1038/s41563-018-0081-x.
(11) Liu, Y.; Cui, J. Y.; Du, K.; Tian, H.; He, Z. F.; Zhou, Q. H.; Yang, Z. L.; Deng, Y. Z.; Chen, D.; Zuo, X. B.; Ren, Y.; Wang, L.; Zhu, H. M.; Zhao, B. D.; Di, D. W.; Wang, J. P.; Friend, R. H.; Jin, Y. Z. Efficient blue light-emitting diodes based on quantum-confined bromide perovskite nanostructures. *Nat Photonics* **2019**, *13* (11), 760-+. DOI: 10.1038/s41566-019-0505-4.
(12) Tsai, H.; Nie, W. Y.; Blancon, J. C.; Stoumpos, C. C.; Soe, C. M. M.; Yoo, J.; Crochet, J.; Tretiak, S.; Even, J.; Sadhanala, A.; Azzellino, G.; Brenes, R.; Ajayan, P. M.; Bulovic, V.; Stranks, S. D.; Friend, R. H.; Kanatzidis, M. G.; Mohite, A. D. Stable Light-Emitting Diodes Using Phase-Pure Ruddlesden-Popper Layered Perovskites. *Advanced Materials* **2018**, *30* (6). DOI: 10.1002/adma.201704217.

(13) Dou, L.; Yang, Y.; You, J.; Hong, Z.; Chang, W.-H.; Li, G.; Yang, Y. Solution-processed hybrid perovskite photodetectors with high detectivity. *Nat Commun* **2014**, *5* (1), 5404. DOI: 10.1038/ncomms6404.
(14) Li, G. H.; Gao, R.; Han, Y.; Zhai, A. P.; Liu, Y. C.; Tian, Y.; Tian, B. N.; Hao, Y. Y.; Liu, S. Z.; Wu, Y. C.; Cui, Y. X. High detectivity photodetectors based on perovskite nanowires with suppressed surface defects. *Photonics Res* **2020**, *8* (12), 1862-1874. DOI: 10.1364/Prj.403030.
(15) Qiao, B. S.; Wang, S. Y.; Zhang, Z. H.; Lian, Z. D.; Zheng, Z. Y.; Wei, Z. P.; Li, L.; Ng, K. W.; Wang, S. P.; Liu, Z. B. Photosensitive Dielectric 2D Perovskite Based Photodetector for Dual Wavelength Demultiplexing. *Advanced Materials* **2023**, *35* (21). DOI: 10.1002/adma.202300632.
(16) Lei, L.; Dong, Q.; Gundogdu, K.; So, F. Metal Halide Perovskites for Laser Applications. *Adv Funct Mater* **2021**, *31* (16). DOI: 10.1002/adfm.202010144.

(17) Quan, L. N.; Rand, B. P.; Friend, R. H.; Mhaisalkar, S. G.; Lee, T. W.; Sargent, E. H. Perovskites for Next-Generation Optical Sources. *Chemical Reviews* **2019**, *119* (12), 7444-7477. DOI: 10.1021/acs.chemrev.9b00107.
(18) Wang, C. H.; Dai, G.; Wang, J. H.; Cui, M. H.; Yang, Y. G.; Yang, S. R.; Qin, C. C.; Chang, S.; Wu, K. F.; Liu, Y. F.; Zhong, H. Z. Low-Threshold Blue Quasi-2D Perovskite Laser through Domain Distribution Control. *Nano Lett* **2022**, *22* (3), 1338-1344. DOI: 10.1021/acs.nanolett.1c04666.
(19) Xu, Z. S.; Han, X.; Wu, W. Q.; Li, F. T.; Wang, R.; Lu, H.; Lu, Q. C.; Ge, B. H.; Cheng, N. Y.; Li, X. Y.; Yao, G. J.; Hong, H.; Liu, K. H.; Pan, C. F. Controlled on-chip fabrication of large-scale perovskite single crystal arrays for high-performance laser and photodetector integration. *Light-Sci Appl* **2023**, *12* (1). DOI: 10.1038/s41377-023-01107-4.

(20) Liu, A.; Zhu, H. H.; Bai, S.; Reo, Y.; Caironi, M.; Petrozza, A.; Dou, L. T.; Noh, Y. Y. High-performance metal halide perovskite transistors. *Nat Electron* **2023**, *6* (8), 559-571. DOI: 10.1038/s41928-023-01001-2.
(21) Vasilopoulou, M.; Yusoff, A. B.; Chai, Y.; Kourtis, M. A.; Matsushima, T.; Gasparini, N.; Du, R.; Gao, F.; Nazeeruddin, M. K.; Anthopoulos, T. D.; Noh, Y. Y. Neuromorphic computing

based on halide perovskites. *Nat Electron* **2023**, *6* (12), 949-962. DOI: 10.1038/s41928-023-01082-z.
(22) Zhang, L. X.; Mei, L. Y.; Wang, K. Y.; Lv, Y. H.; Zhang, S.; Lian, Y. X.; Liu, X. K.; Ma, Z. W.; Xiao, G. J.; Liu, Q.; Zhai, S. B.; Zhang, S. L.; Liu, G. L.; Yuan, L. G.; Guo, B. B.; Chen, Z. M.; Wei, K. Y.; Liu, A. Q.; Yue, S. Z.; Niu, G. D.; Pan, X. Y.; Sun, J.; Hua, Y.; Wu, W. Q.; Di, D. W.; Zhao, B. D.; Tian, J. J.; Wang, Z. J.; Yang, Y.; Chu, L.; Yuan, M. J.; Zeng, H. B.; Yip, H. L.; Yan, K. Y.; Xu, W. T.; Zhu, L.; Zhang, W. H.; Xing, G. C.; Gao, F.; Ding, L. M. Advances in the Application of Perovskite Materials. *Nano-Micro Lett* **2023**, *15* (1). DOI: 10.1007/s40820-023-01140-3.

(23) Abate, A. Perovskite Solar Cells Go Lead Free. *Joule* **2017**, *1* (4), 659-664. DOI: 10.1016/j.joule.2017.09.007.
(24) Li, G.; Liu, Y. T.; Yang, F.; Li, M.; Zhang, Z.; Pascual, J.; Wang, Z. K.; Wei, S. Z.; Zhao, X. Y.; Liu, H. R.; Zhao, J. B.; Lin, C. T.; Li, J. M.; Li, Z.; Abate, A.; Cantone, I. Biotoxicity of Halide Perovskites in Mice. *Advanced Materials* **2024**, *36* (2). DOI: 10.1002/adma.202306860.
(25) Li, J. M.; Cao, H. L.; Jiao, W. B.; Wang, Q.; Wei, M. D.; Cantone, I.; Lu, J.; Abate, A. Biological impact of lead from halide perovskites reveals the risk of introducing a safe threshold. *Nat Commun* **2020**, *11* (1). DOI: 10.1038/s41467-019-13910-y.

(26) Stoumpos, C. C.; Kanatzidis, M. G. The Renaissance of Halide Perovskites and Their Evolution as Emerging Semiconductors. *Accounts Chem Res* **2015**, *48* (10), 2791-2802. DOI: 10.1021/acs.accounts.5b00229.
(27) Eperon, G. E.; Leijtens, T.; Bush, K. A.; Prasanna, R.; Green, T.; Wang, J. T. W.; McMeekin, D. P.; Volonakis, G.; Milot, R. L.; May, R.; Palmstrom, A.; Slotcavage, D. J.; Belisle, R. A.; Patel, J. B.; Parrott, E. S.; Sutton, R. J.; Ma, W.; Moghadam, F.; Conings, B.; Babayigit, A.; Boyen, H. G.; Bent, S.; Giustino, F.; Herz, L. M.; Johnston, M. B.; McGehee, M. D.; Snaith, H. J. Perovskite-perovskite tandem photovoltaics with optimized band gaps. *Science* **2016**, *354* (6314), 861-865. DOI: 10.1126/science.aaf9717.
(28) Ma, L.; Hao, F.; Stoumpos, C. C.; Phelan, B. T.; Wasielewski, M. R.; Kanatzidis, M. G. Carrier Diffusion Lengths of over 500 nm in Lead-Free Perovskite CHNHSnI Films. *J Am Chem Soc* **2016**, *138* (44), 14750-14755. DOI: 10.1021/jacs.6b09257.

(29) Stoumpos, C. C.; Malliakas, C. D.; Kanatzidis, M. G. Semiconducting Tin and Lead Iodide Perovskites with Organic Cations: Phase Transitions, High Mobilities, and Near-Infrared Photoluminescent Properties. *Inorg Chem* **2013**, *52* (15), 9019-9038. DOI: 10.1021/ic401215x.
(30) Hossain, T.; Joy, S.; Draffen, K.; Bright, R.; Johnson, S.; Graham, K. R. Oxidation in Tin Halide Perovskites: Influence of Acidic and Basic Additives. *ACS Applied Energy Materials* **2023**, *6* (24), 12334-12342. DOI: 10.1021/acsaem.3c02150.
(31) Liu, J. K.; Yao, H. H.; Wang, S. R.; Wu, C.; Ding, L. M.; Hao, F. Origins and Suppression of Sn(II)/Sn(IV) Oxidation in Tin Halide Perovskite Solar Cells. *Adv Energy Mater* **2023**, *13* (23). DOI: 10.1002/aenm.202300696.
(32) Kumar, M. H.; Dharani, S.; Leong, W. L.; Boix, P. P.; Prabhakar, R. R.; Baikie, T.; Shi, C.; Ding, H.; Ramesh, R.; Asta, M.; Graetzel, M.; Mhaisalkar, S. G.; Mathews, N. Lead-Free Halide Perovskite Solar Cells with High Photocurrents Realized Through Vacancy Modulation. *Advanced Materials* **2014**, *26* (41), 7122-+. DOI: 10.1002/adma.201401991.

(33) Mitzi, D. B.; Feild, C. A.; Schlesinger, Z.; Laibowitz, R. B. Transport, Optical, and Magnetic-Properties of the Conducting Halide Perovskite Ch3nh3sni3. *J Solid State Chem* **1995**, *114* (1), 159-163. DOI: DOI 10.1006/jssc.1995.1023.
(34) Takahashi, Y.; Hasegawa, H.; Takahashi, Y.; Inabe, T. Hall mobility in tin iodide perovskite CHNHSnI: Evidence for a doped semiconductor. *J Solid State Chem* **2013**, *205*, 39-43. DOI: 10.1016/j.jssc.2013.07.008.

(35) Takahashi, Y.; Obara, R.; Lin, Z. Z.; Takahashi, Y.; Naito, T.; Inabe, T.; Ishibashi, S.; Terakura, K. Charge-transport in tin-iodide perovskite CHNHSnI: origin of high conductivity. *Dalton T* **2011**, *40* (20), 5563-5568. DOI: 10.1039/c0dt01601b.

(36) Mitzi, D. B.; Feild, C. A.; Harrison, W. T. A.; Guloy, A. M. Conducting Tin Halides with a Layered Organic-Based Perovskite Structure. *Nature* **1994**, *369* (6480), 467-469. DOI: DOI 10.1038/369467a0.
(37) Cao, Q. L.; Li, P. W.; Chen, W.; Zang, S. Q.; Han, L. Y.; Zhang, Y. Q.; Song, Y. L. Two-dimensional perovskites: Impacts of species, components, and properties of organic spacers on solar cells. *Nano Today* **2022**, *43*. DOI:10.1016/j.nantod.2022.101394.

(38) Forlano, K. M.; Roy, C. R.; Mihalyi-Koch, W.; Hossain, T.; Sanders, K.; Guzei, I.; Graham, K. R.; Wright, J. C.; Jin, S. High Layer Number (n = 1–6) 2D Ruddlesden–Popper Lead Bromide Perovskites: Nanosheets, Crystal Structure, and Optoelectronic Properties. *Acs Mater Lett* **2023**, *5* (11), 2913-2921. DOI: 10.1021/acsmaterialslett.3c00809.
(39) Zhang, T. J.; Zhou, C. C.; Feng, X. Z.; Dong, N. N.; Chen, H.; Chen, X. F.; Zhang, L.; Lin, J.; Wang, J. Regulation of the luminescence mechanism of two-dimensional tin halide perovskites. *Nat Commun* **2022**, *13* (1). DOI: 10.1038/s41467-021-27663-0.
(40) Li, X. T.; Hoffman, J. M.; Kanatzidis, M. G. The 2D Halide Perovskite Rulebook: How the Spacer Influences Everything from the Structure to Optoelectronic Device Efficiency. *Chemical Reviews* **2021**, *121* (4), 2230-2291. DOI: 10.1021/acs.chemrev.0c01006.
(41) Mitzi, D. B.; Dimitrakopoulos, C. D.; Kosbar, L. L. Structurally tailored organic-inorganic perovskites: Optical properties and solution-processed channel materials for thin-film transistors. *Chemistry of Materials* **2001**, *13* (10), 3728-3740. DOI: 10.1021/cm010105g.
(42) Blancon, J. C.; Stier, A. V.; Tsai, H.; Nie, W.; Stoumpos, C. C.; Traore, B.; Pedesseau, L.; Kepenekian, M.; Katsutani, F.; Noe, G. T.; Kono, J.; Tretiak, S.; Crooker, S. A.; Katan, C.; Kanatzidis, M. G.; Crochet, J. J.; Even, J.; Mohite, A. D. Scaling law for excitons in 2D perovskite quantum wells. *Nat Commun* **2018**, *9*. DOI: 10.1038/s41467-018-04659-x.

(43) Yan, L. F.; Ma, J. J.; Li, P. W.; Zang, S. Q.; Han, L. Y.; Zhang, Y. Q.; Song, Y. L. Charge-Carrier Transport in Quasi-2D Ruddlesden-Popper Perovskite Solar Cells. *Advanced Materials* **2022**, *34* (7). DOI: 10.1002/adma.202106822.

(44) Cao, D. H.; Stoumpos, C. C.; Farha, O. K.; Hupp, J. T.; Kanatzidis, M. G. 2D Homologous Perovskites as Light-Absorbing Materials for Solar Cell Applications. *J Am Chem Soc* **2015**, *137* (24), 7843-7850. DOI: 10.1021/jacs.5b03796.
(45) Li, P. W.; Liu, X. L.; Zhang, Y. Q.; Liang, C.; Chen, G. S.; Li, F. Y.; Su, M.; Xing, G. C.; Tao, X. T.; Song, Y. L. Low-Dimensional Dion-Jacobson-Phase Lead-Free Perovskites for High-Performance Photovoltaics with Improved Stability. *Angew Chem Int Edit* **2020**, *59* (17), 6909-6914. DOI: 10.1002/anie.202000460.

(46) Liao, Y. Q.; Liu, H. F.; Zhou, W. J.; Yang, D. W.; Shang, Y. Q.; Shi, Z. F.; Li, B. H.; Jiang, X. Y.; Zhang, L. J.; Quan, L. N.; Quintero-Bermudez, R.; Sutherland, B. R.; Mi, Q. X.; Sargent, E. H.; Ning, Z. L. Highly Oriented Low-Dimensional Tin Halide Perovskites with Enhanced Stability and Photovoltaic Performance. *J Am Chem Soc* **2017**, *139* (19), 6693-6699. DOI: 10.1021/jacs.7b01815.
(47) Quan, L. N.; Yuan, M. J.; Comin, R.; Voznyy, O.; Beauregard, E. M.; Hoogland, S.; Buin, A.; Kirmani, A. R.; Zhao, K.; Amassian, A.; Kim, D. H.; Sargent, E. H. Ligand-Stabilized Reduced-Dimensionality Perovskites. *J Am Chem Soc* **2016**, *138* (8), 2649-2655. DOI: 10.1021/jacs.5b11740.
(48) Yuan, F. F.; Liang, Y. C.; Miao, Z. P.; Zhang, T.; Zhao, R. D.; Peng, S. H.; Xie, Y. H.; Liang, W. L.; Zhu, H.; Li, P. W.; Zhang, Y. Q.; Song, Y. L. Oxygen-Containing Diamine Cations Enable Highly Efficient and Stable 2D Dion-Jacobson Perovskite Solar Cells. *Chemistry of Materials* **2024**, *36* (3), 1621-1630. DOI: 10.1021/acs.chemmater.3c02960.
(49) Zhu, H.; Ma, J. J.; Li, P. W.; Zang, S. Q.; Zhang, Y. Q.; Song, Y. L. Low-dimensional Sn-based perovskites: Evolution and future prospects of solar cells. *Chem-Us* **2022**, *8* (11), 2939-2960. DOI: 10.1016/j.chempr.2022.07.027.
(50) Jang, Y. W.; Lee, S.; Yeom, K. M.; Jeong, K.; Choi, K.; Choi, M.; Noh, J. H. Intact 2D/3D halide junction perovskite solar cells via solid-phase in-plane growth. *Nature Energy* **2021**, *6* (1), 63-+. DOI: 10.1038/s41560-020-00749-7.
(51) Wang, G.; Wang, C.; MacKenzie, R. C. I.; Zhu, Z. H.; Chen, Y.; Ruan, S. P.; Wen, S. P. Using Ligand Engineering to Produce Efficient and Stable Pb-Sn Perovskite Solar Cells with Antioxidative 2D Capping Layers. *Acs Appl Mater Inter* **2022**, *14* (12), 14729-14738. DOI: 10.1021/acsami.1c24763.
(52) Wei, M. Y.; Xiao, K.; Walters, G.; Lin, R. X.; Zhao, Y. B.; Saidaminov, M. I.; Todorovic, P.; Johnston, A.; Huang, Z. R.; Chen, H. J.; Li, A. D.; Zhu, J.; Yang, Z. Y.; Wang, Y. K.; Proppe, A. H.; Kelley, S. O.; Hou, Y.; Voznyy, O.; Tan, H. R.; Sargent, E. H. Combining Efficiency and Stability in Mixed Tin-Lead Perovskite Solar Cells by Capping Grains with an Ultrathin 2D Layer. *Advanced Materials* **2020**, *32* (12). DOI:10.1002/adma.201907058.

(53) Chao, I. H.; Yang, Y. T.; Yu, M. H.; Chen, C. H.; Liao, C. H.; Lin, B. H.; Ni, I. C.; Chen, W. C.; Ho-Baillie, A. W. Y.; Chueh, C. C. Performance Enhancement of Lead-Free 2D Tin Halide Perovskite Transistors by Surface Passivation and Its Impact on Non-Volatile Photomemory Characteristics. *Small* **2023**, *19* (20). DOI: 10.1002/smll.202207734.
(54) Cho, J. H.; Go, J. Y.; Bui, T. T.; Mun, S.; Kim, Y.; Ahn, K.; Noh, Y. Y.; Kim, M. G. Anion-Vacancy-Defect Passivation of a 2D-Layered Tin-Based Perovskite Thin-Film Transistor with Sulfur Doping. *Adv Electron Mater* **2023**, *9* (3). DOI: 10.1002/aelm.202201014.
(55) Go, J. Y.; Zhu, H.; Reo, Y.; Kim, H.; Liu, A.; Noh, Y. Y. Sodium Incorporation for Enhanced Performance of Two-Dimensional Sn-Based Perovskite Transistors. *Acs Appl Mater Inter* **2022**, *14* (7), 9363-9367. DOI: 10.1021/acsami.1c19368.
(56) Li, L. T.; Liu, X.; Guo, J. H.; Ji, H. Y.; Zhang, F.; Lou, Z. D.; Qin, L.; Hu, Y. F.; Hou, Y. B.; Teng, F. Low-Operating-Voltage Two-Dimensional Tin Perovskite Field-Effect Transistors with Multilayer Gate Dielectrics Based on a Fluorinated Copolymer. *J Phys Chem Lett* **2023**, *14* (8), 2223-2233. DOI: 10.1021/acs.jpclett.3c00072.
(57) Liu, X.; Ji, H. Y.; Li, L. T.; Zhang, F.; Guo, J. H.; Qin, L.; Lou, Z. D.; Li, D.; Hu, Y. F.; Hou, Y. B.; Teng, F. Two-Dimensional Layered Simple Aliphatic Monoammonium Tin Perovskite Thin Films and Potential Applications in Field-Effect Transistors. *Acs Appl Mater Inter* **2022**, *14* (44), 50401-50413. DOI: 10.1021/acsami.2c15044.

(58) Lanzetta, L.; Marin-Beloqui, J. M.; Sanchez-Molina, I.; Ding, D.; Haque, S. A. Two-Dimensional Organic Tin Halide Perovskites with Tunable Visible Emission and Their Use in Light-Emitting Devices. *Acs Energy Lett* **2017**, *2* (7), 1662-1668. DOI: 10.1021/acsenergylett.7b00414.
(59) Wang, C. H.; Cui, S. Q.; Ju, Y. Y.; Chen, Y.; Chang, S.; Zhong, H. Z. Color-Stable Two-Dimensional Tin-Based Perovskite Light-Emitting Diodes: Passivation Effects of Diphenylphosphine Oxide Derivatives. *Adv Funct Mater* **2023**, *33* (29). DOI: 10.1002/adfm.202301304.
(60) Wang, Z. B.; Wang, F. Z.; Zhao, B.; Qu, S. N.; Hayat, T.; Alsaedi, A.; Sui, L. Z.; Yuan, K. J.; Zhang, J. Q.; Wei, Z. X.; Tan, Z. A. Efficient Two-Dimensional Tin Halide Perovskite Light-Emitting Diodes via a Spacer Cation Substitution Strategy. *J Phys Chem Lett* **2020**, *11* (3), 1120-+. DOI: 10.1021/acs.jpclett.9b03565.
(61) Yuan, F. L.; Zheng, X. P.; Johnston, A.; Wang, Y. K.; Zhou, C.; Dong, Y. T.; Chen, B.; Chen, H. J.; Fan, J. Z.; Sharma, G.; Li, P. C.; Gao, Y.; Voznyy, O.; Kung, H. T.; Lu, Z. H.; Bakr, O. M.; Sargent, E. H. Color-pure red light-emitting diodes based on two-dimensional lead-free perovskites. *Sci Adv* **2020**, *6* (42). DOI: 10.1126/sciadv.abb0253.

(62) Alvarado-Leaños, A. L.; Cortecchia, D.; Saggau, C. N.; Martani, S.; Folpini, G.; Feltri, E.; Albaqami, M. D.; Ma, L. B.; Petrozza, A. Lasing in Two-Dimensional Tin Perovskites. *Acs Nano* **2022**, *16* (12), 20671-20679. DOI: 10.1021/acsnano.2c07705.
(63) Ding, G. C.; He, X. X.; Zhang, H. H.; Fu, H. B. Ethanol-assisted synthesis of two-dimensional tin(ii) halide perovskite single crystals for amplified spontaneous emission. *J Mater Chem C* **2022**, *10* (30), 10902-10907. DOI: 10.1039/d2tc01873j.
(64) Li, Y. H.; Zhou, H. Z.; Xia, M.; Shen, H. Z.; Wang, T. Y.; Gao, H. K.; Sheng, X.; Han, Y. X.; Chen, Z.; Dou, L. T.; Zhu, H. M.; Shi, E. Z. Phase-pure 2D tin halide perovskite thin flakes for stable lasing. *Sci Adv* **2023**, *9* (32). DOI: 10.1126/sciadv.adh0517.

(65) Ghosh, S.; Kumar, J.; Nim, G. K.; Bag, M.; Kar, P. Air stable highly luminescent 2D tin halide perovskite nanocrystals as photodetectors. *Chem Commun* **2023**, *59* (15), 2110-2113. DOI: 10.1039/d3cc00097d.
(66) Han, C. C.; Wei, Q.; Jiang, X. Y.; Yao, B.; Li, H. S.; Chen, H.; Li, B. H.; Fu, P. F.; Zhou, W. J.; Ning, Z. J. Large-Size and Polarization-Sensitive Two-Dimensional Sn Perovskite Single Crystals. *Acs Mater Lett* **2022**, *4* (5), 987-994. DOI: 10.1021/acsmaterialslett.2c00163.
(67) Park, I. H.; Chu, L. Q.; Leng, K.; Choy, Y. F.; Liu, W.; Abdelwahab, I.; Zhu, Z. Y.; Ma, Z. R.; Chen, W.; Xu, Q. H.; Eda, G.; Loh, K. P. Highly Stable Two-Dimensional Tin(II) Iodide Hybrid Organic-Inorganic Perovskite Based on Stilbene Derivative. *Adv Funct Mater* **2019**, *29* (39). DOI: 10.1002/adfm.201904810.

(68) Cao, J. T.; Guo, Z.; Zhu, S.; Fu, Y. Y.; Zhang, H.; Wang, Q.; Gu, Z. J. Preparation of Lead-free Two-Dimensional-Layered (CHNH)SnBr Perovskite Scintillators and Their Application in X-ray Imaging. *Acs Appl Mater Inter* **2020**, *12* (17), 19797-19804. DOI: 10.1021/acsami.0c02116.

(69) Li, M. B.; He, Y. H.; Feng, X. P.; Qu, W.; Wei, W.; Yang, B.; Wei, H. T. Reductant Engineering in Stable and High-Quality Tin Perovskite Single Crystal Growth for Heterojunction X-Ray Detectors. *Advanced Materials* **2023**. DOI: 10.1002/adma.202307042.
(70) Zheng, H. Y.; Liu, G. Z.; Zhu, L. Z.; Ye, J. J.; Zhang, X. H.; Alsaedi, A.; Hayat, T.; Pan, X.; Dai, S. Y. The Effect of Hydrophobicity of Ammonium Salts on Stability of Quasi-2D

Perovskite Materials in Moist Condition. *Adv Energy Mater* **2018**, *8* (21). DOI: 10.1002/aenm.201800051.

(71) Fu, W. F.; Liu, H. B.; Shi, X. L.; Zuo, D.; Li, X. S.; Jen, L. K. Y. Tailoring the Functionality of Organic Spacer Cations for Efficient and Stable Quasi-2D Perovskite Solar Cells. *Adv Funct Mater* **2019**, *29* (25). DOI: 10.1002/adfm.201900221.

(72) Park, S. M.; Wei, M. Y.; Xu, J.; Atapattu, H. R.; Eickemeyer, F. T.; Darabi, K.; Grater, L.; Yang, Y.; Liu, C.; Teale, S.; Chen, B.; Chen, H.; Wang, T. H.; Zeng, L. W.; Maxwell, A.; Wang, Z. W.; Rao, K. R.; Cai, Z. Y.; Zakeeruddin, S. M.; Pham, J. T.; Risko, C. M.; Amassian, A.; Kanatzidis, M. G.; Graham, K. R.; Grätzel, M.; Sargent, E. H. Engineering ligand reactivity enables high-temperature operation of stable perovskite solar cells. *Science* **2023**, *381* (6654), 209-215. DOI: 10.1126/science.adi4107.
(73) Shi, J.; Gao, Y.; Gao, X.; Zhang, Y.; Zhang, J.; Jing, X.; Shao, M. Fluorinated Low-Dimensional Ruddlesden–Popper Perovskite Solar Cells with over 17% Power Conversion Efficiency and Improved Stability. *Advanced Materials* **2019**, *31* (37), 1901673. DOI: 10.1002/adma.201901673.
(74) Li, P. W.; Yan, L. F.; Cao, Q. L.; Liang, C.; Zhu, H.; Peng, S. H.; Yang, Y. P.; Liang, Y. C.; Zhao, R. D.; Zang, S. Q.; Zhang, Y. Q.; Song, Y. L. Dredging the Charge-Carrier Transfer Pathway for Efficient Low-Dimensional Ruddlesden-Popper Perovskite Solar Cells. *Angew Chem Int Edit* **2023**, *62* (13). DOI: 10.1002/anie.202217910.
(75) Mosconi, E.; Alothman, A. A.; Long, R.; Kaiser, W.; De Angelis, F. Intermolecular Interactions of A-Site Cations Modulate Stability of 2D Metal Halide Perovskites. *Acs Energy Lett* **2023**, *8* (1), 748-752. DOI: 10.1021/acsenergylett.2c02742.
(76) Triggs, C. T.; Ross, R. D.; Mihalyi-Koch, W.; Clewett, C. F. M.; Sanders, K. M.; Guzei, I. A.; Jin, S. Spacer Cation Design Motifs for Enhanced Air Stability in Lead-Free 2D Tin Halide Perovskites. *Acs Energy Lett* **2024**. DOI: 10.1021/acsenergylett.4c00615.
(77) Zhang, T.; Miao, Z. P.; Zhao, R. D.; Yuan, F. F.; Peng, S. H.; Liang, Y. C.; Zhu, H.; Xie, Y. H.; Liang, W. L.; Li, P. W.; Zhang, Y. Q.; Song, Y. L. Optimization Charge-Carrier Properties of 2D Ruddlesden-Popper Perovskite for Solar Cells. *Acs Energy Lett* **2024**, *9* (5), 2248-2256. DOI: 10.1021/acsenergylett.4c00724.
(78) Krause, L.; Herbst-Irmer, R.; Sheldrick, G. M.; Stalke, D. Comparison of silver and molybdenum microfocus X-ray sources for single-crystal structure determination. *J Appl Crystallogr* **2015**, *48*, 3-10. DOI: 10.1107/S1600576714022985.
(79) Parkin, S.; Moezzi, B.; Hope, H. Xabs2 - an Empirical Absorption Correction Program. *J Appl Crystallogr* **1995**, *28*, 53-56. DOI: Doi 10.1107/S0021889894009428.
(80) Sheldrick, G. M. - Integrated space-group and crystal-structure determination. *Acta Crystallogr A* **2015**, *71*, 3-8. DOI: 10.1107/S2053273314026370.
(81) Sheldrick, G. M. Crystal structure refinement with. *Acta Crystallogr C* **2015**, *71*, 3-8. DOI: 10.1107/S2053229614024218.
(82) Wilson, A. J. C.; Geist, V. International Tables for Crystallography. Volume C: Mathematical, Physical and Chemical Tables. Kluwer Academic Publishers, Dordrecht/Boston/London 1992 (published for the International Union of Crystallography), 883 Seiten, ISBN 0-792-3-16-38X. *Crystal Research and Technology* **1993**, *28* (1), 110-110. DOI: https://doi.org/10.1002/crat.2170280117.

(83) Knutson, J. L.; Martin, J. D.; Mitzi, D. B. Tuning the Band Gap in Hybrid Tin Iodide Perovskite Semiconductors Using Structural Templating. *Inorg Chem* **2005**, *44* (13), 4699-4705. DOI: 10.1021/ic050244q.
(84) Mao, L.; Tsai, H.; Nie, W.; Ma, L.; Im, J.; Stoumpos, C. C.; Malliakas, C. D.; Hao, F.; Wasielewski, M. R.; Mohite, A. D.; Kanatzidis, M. G. Role of Organic Counterion in Lead- and Tin-Based Two-Dimensional Semiconducting Iodide Perovskites and Application in Planar Solar Cells. *Chem. Mater.* **2016**, *28* (21), 7781-7792. DOI: 10.1021/acs.chemmater.6b03054.
(85) Mitzi, D. B. Synthesis, Crystal Structure, and Optical and Thermal Properties of (C4H9NH3)2MI4 (M = Ge, Sn, Pb). *Chem. Mater.* **1996**, *8* (3), 791-800. DOI: 10.1021/cm9505097.
(86) Reo, Y.; Choi, T.; Go, J. Y.; Jeon, S.; Lim, B.; Zhu, H. H.; Liu, A.; Noh, Y. Y. Precursor Solution Aging: A Universal Strategy Modulating Crystallization of Two-Dimensional Tin Halide Perovskite Films. *Acs Energy Lett* **2023**, *8* (7), 3088-3094. DOI: 10.1021/acsenergylett.3c00694.
(87) Lanzetta, L.; Webb, T.; Zibouche, N.; Liang, X.; Ding, D.; Min, G.; Westbrook, R. J. E.; Gaggio, B.; Macdonald, T. J.; Islam, M. S.; Haque, S. A. Degradation mechanism of hybrid tin-based perovskite solar cells and the critical role of tin (IV) iodide. *Nat Commun* **2021**, *12* (1), 2853. DOI: 10.1038/s41467-021-22864-z.
(88) Li, L.; Rao, H.; Wu, Z.; Hong, J.; Zhang, J.; Pan, Z.; Zhong, X. Moisture Induced Secondary Crystal Growth Boosting the Efficiency of Hole Transport Layer-Free Carbon-Based Perovskite Solar Cells beyond 19.5%. *Adv Funct Mater* **2024**, *34* (1), 2308428. DOI: https://doi.org/10.1002/adfm.202308428.
(89) Liu, K.; Luo, Y.; Jin, Y.; Liu, T.; Liang, Y.; Yang, L.; Song, P.; Liu, Z.; Tian, C.; Xie, L.; Wei, Z. Moisture-triggered fast crystallization enables efficient and stable perovskite solar cells. *Nat Commun* **2022**, *13* (1), 4891. DOI: 10.1038/s41467-022-32482-y.
(90) You, J.; Yang, Y.; Hong, Z.; Song, T.-B.; Meng, L.; Liu, Y.; Jiang, C.; Zhou, H.; Chang, W.-H.; Li, G.; Yang, Y. Moisture assisted perovskite film growth for high performance solar cells. *Applied Physics Letters* **2014**, *105* (18). DOI: 10.1063/1.4901510 (acccessed 2/20/2024).
(91) Ahn, N.; Kwak, K.; Jang, M. S.; Yoon, H.; Lee, B. Y.; Lee, J.-K.; Pikhitsa, P. V.; Byun, J.; Choi, M. Trapped charge-driven degradation of perovskite solar cells. *Nat Commun* **2016**, *7* (1), 13422. DOI: 10.1038/ncomms13422.
(92) Frost, J. M.; Butler, K. T.; Brivio, F.; Hendon, C. H.; van Schilfgaarde, M.; Walsh, A. Atomistic Origins of High-Performance in Hybrid Halide Perovskite Solar Cells. *Nano Lett* **2014**, *14* (5), 2584-2590. DOI: 10.1021/nl500390f.
(93) Huang, W.; Manser, J. S.; Kamat, P. V.; Ptasinska, S. Evolution of Chemical Composition, Morphology, and Photovoltaic Efficiency of CH3NH3PbI3 Perovskite under Ambient Conditions. *Chemistry of Materials* **2016**, *28* (1), 303-311. DOI: 10.1021/acs.chemmater.5b04122.

- **Table of Contents Figure**

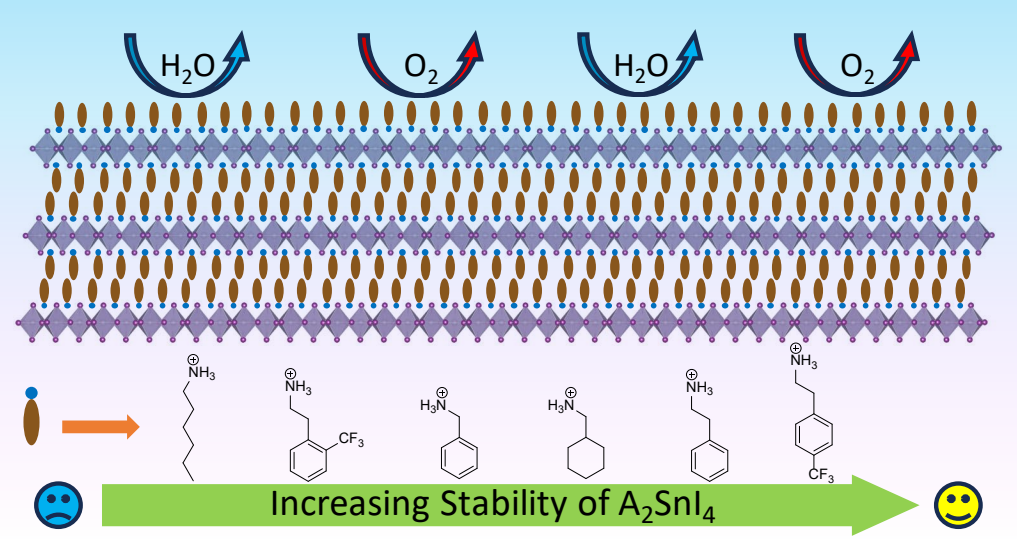
H2O
O2
H2O
O2
NH3
NH3
CF3
H3N
H3N
NH3
NH3
CF3
Increasing Stability of A2SnI4